Journal of Biomedical Optics

BiomedicalOptics.SPIEDigitalLibrary.org

Morphometric analysis of erythrocytes from patients with thalassemia using tomographic diffractive microscopy

Yang-Hsien Lin
Shin-Shyang Huang
Shang-Ju Wu
Kung-Bin Sung

SPIE.

Yang-Hsien Lin, Shin-Shyang Huang, Shang-Ju Wu, Kung-Bin Sung, "Morphometric analysis of erythrocytes from patients with thalassemia using tomographic diffractive microscopy," *J. Biomed. Opt.* **22**(11), 116009 (2017), doi: 10.1117/1.JBO.22.11.116009.

Morphometric analysis of erythrocytes from patients with thalassemia using tomographic diffractive microscopy

Yang-Hsien Lin,[a] Shin-Shyang Huang,[a] Shang-Ju Wu,[b] and Kung-Bin Sung[a,c,d,*]
[a]National Taiwan University, Graduate Institute of Biomedical Electronics and Bioinformatics, Taiwan
[b]National Taiwan University Hospital, Department of Internal Medicines, Taiwan
[c]National Taiwan University, Department of Electrical Engineering, Taiwan
[d]National Taiwan University, Molecular Imaging Center, Taiwan

Abstract. Complete blood count is the most common test to detect anemia, but it is unable to obtain the abnormal shape of erythrocytes, which highly correlates with the hematologic function. Tomographic diffractive microscopy (TDM) is an emerging technique capable of quantifying three-dimensional (3-D) refractive index (RI) distributions of erythrocytes without labeling. TDM was used to characterize optical and morphological properties of 172 erythrocytes from healthy volunteers and 419 erythrocytes from thalassemic patients. To efficiently extract and analyze the properties of erythrocytes, we developed an adaptive region-growing method for automatically delineating erythrocytes from 3-D RI maps. The thalassemic erythrocytes not only contained lower hemoglobin content but also showed doughnut shape and significantly lower volume, surface area, effective radius, and average thickness. A multi-indices prediction model achieved perfect accuracy of diagnosing thalassemia using four features, including the optical volume, surface-area-to-volume ratio, sphericity index, and surface area. The results demonstrate the ability of TDM to provide quantitative, hematologic measurements and to assess morphological features of erythrocytes to distinguish healthy and thalassemic erythrocytes. [DOI: 10.1117/1.JBO.22.11.116009]

Keywords: erythrocyte; thalassemia; tomographic diffractive microscopy; three-dimensional adaptive region-growing.

Paper 170474R received Jul. 22, 2017; accepted for publication Nov. 13, 2017; published online Nov. 29, 2017.

1 Introduction

Erythrocytes, commonly known as red blood cells (RBCs), are biconcave in shape to facilitate the diffusion of oxygen and carbon dioxide into and out of the cell. Previous studies have indicated that altered RBC morphology is an important feature in distinguishing a variety of blood-related diseases in the field of hematology.[1] In intrinsic hemolytic anemia such as hereditary spherocytosis, hereditary elliptocytosis, sickle-cell disease, and thalassemia, RBCs show abnormal membrane structure and hemoglobin configuration due to genetic defects and cause-related symptoms in patients.[2,3] For example, thalassemia causes ineffective erythropoiesis and hemolysis, and the severity of thalassemia is determined by the accumulation of abnormal RBCs with defective α/β globin chains.[4]

Complete blood count is the most common test used to diagnose anemia by measuring the physiological and biochemical properties such as the size, count, and hemoglobin content of RBCs. However, the detailed morphological information about individual cells is unavailable in conventional complete blood count results. For analyzing the shape of RBCs, peripheral blood smear is obtained, stained, and examined with bright-field microscopy. However, the contrast is mainly provided by staining, which is qualitative and may alter the morphology of RBCs. Several advanced optical techniques have been developed to obtain more detailed morphological information of RBCs. In defocusing microscopy, the contrast between bright-field images captured at two different focal planes is used to calculate the RBC thickness profile and volume.[5] To get the precise shape of the RBC, it is necessary to know the refractive index (RI) of the RBC, which can be estimated by imaging a small polystyrene bead in the same field of view as the RBC. However, in clinical applications where RIs of diseased RBCs are highly variable between individual RBCs, it is impractical to measure the RI of each RBC. Scanning flow cytometer (SFC) is a high-throughput technique that automatically quantifies the morphology, RI, and hemoglobin content of individual RBCs at the rate of hundreds of cells per second, making it suitable for clinical applications.[6,7] SFC obtains the RBC information by fitting measured angular light scattering patterns of RBCs with theoretical values that are obtained using models of normal RBC shape based on minimization of bending energy of the membrane and assumptions about symmetry of RBC shape. Further efforts are needed to extend SFC to profiling diseased RBCs that often present abnormal and/or nonsymmetrical shapes. Similar approaches have been reported to extract the RBC diameter based on angular light scattering patterns of RBCs in microfluidic flows[8] and to extract the volume and surface area of RBCs from polarization characteristics of scattered light.[9] These two methods are limited to known and fixed shapes of RBCs and do not provide RI information.

Recently, label-free quantitative phase imaging (QPI) techniques have been developed to obtain two-dimensional (2-D) phase images, $\phi(x,y) = (2\pi/\lambda)\int[n(x,y,z) - n_0]\mathrm{d}z$, of individual cells and tissue slices, where λ is the wavelength of the light

*Address all correspondence to: Kung-Bin Sung, E-mail: kbsung@ntu.edu.tw

1083-3668/2017/$25.00 © 2017 SPIE

source, $n(x,y,z)$ and n_0 are the local RI of the specimen and the RI of the medium, respectively.[10,11] Integrating the phase over the whole area of an RBC phase image yields the so-called optical volume (OV), $\mathrm{OV} = (\lambda/2\pi)\iint \phi(x,y)\mathrm{d}x\,\mathrm{d}y = (\lambda/2\pi)\iiint[n(x,y,z) - n_0]\mathrm{d}z\,\mathrm{d}x\,\mathrm{d}y$.[12] For a homogeneous solution, the increase in RI over the medium RI (n_0) is proportional to the mass density or concentration of the solute molecule and is formulated as $n - n_0 = \alpha C$, where α is the RI increment factor and C is the mass density of the solute, respectively.[13] Therefore, the OV calculated from an RBC phase image has been proposed to assess the dry mass of the hemoglobin in the RBC, assuming that hemoglobin is the dominant constituent of RBCs.[10]

The physical thickness and three-dimensional (3-D) RI maps of RBCs can be reconstructed from multiple 2-D phase images acquired at various illumination directions using diffraction tomography techniques.[14] Recently, studies have characterized 3-D morphological indices of RBCs including the surface area, volume, and sphericity and have demonstrated significant differences between RBCs from the cord blood of newborn infants and that of maternal or nonpregnant women[15] and between normal RBCs and RBCs from patients with diabetes mellitus,[16] malaria,[14] iron-deficiency anemia,[17] reticulocytes,[17] hereditary spherocytosis,[17] and sickle-cell disease.[11,17–19] These 3-D RBC parameters provide additional morphometrics for hematologists to better distinguish and understand blood diseases related to deformation of RBCs.

To fully exploit the advantages of QPI and diffraction tomography techniques for quantifying the hemoglobin content and morphological properties of RBCs, it is essential to delineate individual RBCs from 2-D phase images or 3-D RI maps, which is very time-consuming if done manually due to the huge data size. Moon et al. applied the marker-control watershed algorithm to automatically segment RBCs from 2-D quantitative phase images.[20–23] From segmented 2-D RBC images, they estimated various 2-D morphological features.[21] Classifying three typical RBC shapes including stomatocyte, discocyte, and echinocyte using the extracted features was also demonstrated.[23] However, a precise and automatic tool to delineate 3-D RI maps and obtain 3-D morphological properties efficiently is not available.

In this paper, we focused on characterizing the OV and 3-D morphological information of RBCs from patients with thalassemia, one type of hereditary hemoglobinopathy with high prevalence in the world. Morphological features of thalassemic RBCs have not been thoroughly studied without staining. We employed a nearly common-path tomographic microscope recently developed by our group to acquire 3-D RI maps of RBCs obtained from 7 healthy subjects and 27 thalassemic patients. An automatic segmentation method was developed, validated with a numerical phantom, and applied to delineate the 3-D RI maps of the RBCs. We then quantified the OV and various morphological indices of the RBCs. The diagnostic accuracy of using these indices to distinguish thalassemic RBCs from normal RBCs, both at the single-cell level and on the per-patient basis, is presented.

2 Materials and Methods

2.1 *RBCs Images Acquisition*

To construct a 3-D RI map of an RBC, we acquired a series of 2-D amplitude/phase images of the RBC using a nearly common-path tomographic diffractive microscope (cTDM). The details of the system setup were described in a previous publication.[24] Briefly, cTDM uses a 532-nm continuous-wave laser to illuminate a semitransparent specimen with a collimated beam. The beam diameter is at least seven times larger than the diameter of the object and constant throughout the thickness of the object. The incident angle is scanned by a single-axis galvanometer mirror (Nutfield Technology Inc.) to be in the range of −65 deg to 65 deg in the medium. The transmitted field through the specimen is collected by an objective lens (Olympus UPLSAPO 100XO, 1.4 NA), interfered with a uniform reference beam, and imaged by a high-speed CMOS camera (GZL-CL-41C6M-C, Gazelle, Point Grey) with a transverse magnification of about 85. The reference beam is generated by a transmission grating located near an intermediate image plane of the objective lens.[25] The amplitude/phase images are retrieved from the interference images by band-pass filtering in the spatial frequency domain without zero-padding, followed by a Fourier-based phase unwrapping method.[26,27] 3-D RI maps are reconstructed iteratively based on optical diffraction tomography with direct interpolation in the Fourier domain and the positivity constraint.[28] All of the phase retrieval and 3-D reconstruction steps were performed on graphic processing units. To assess the spatial resolution of cTDM, we extracted cross sectional RI images through the center of the reconstructed RI tomogram of a specimen and profiled RI distributions along the optical axis and transverse directions. The edge response, defined as the distance between 10% and 90% of the maximum RI above the medium RI, was computed. The edge responses in the transverse and axial directions of RI images of 10 μm polystyrene beads were 0.35 and 1.5 μm, respectively. The axial edge response estimated from RI images of RBCs was about 1.0 μm. The voxel size of a reconstructed 3-D RI tomogram was $0.129 \times 0.129 \times 0.129$ (μm^3). Figure 1 shows a representative RI distribution of a normal RBC in three orthogonal sections.

2.2 *RBC Sample Preparation and Data Acquisition*

This study was approved by the Institutional Review Board of National Taiwan University Hospital, and an informed consent was obtained from each subject. We collected 172 hematologically normal RBCs from seven healthy subjects (six males, one female, mean age 23 ± 2 y/o) and 419 thalassemic RBCs from 27 adult thalassemia-minor patients (14 males, 13 female, mean age 59 ± 15 y/o). All patients had not received blood transfusions for at least 2 months prior to the time of participating the study. After the blood was drawn from a subject, it was stored in anticoagulant at room temperature (22°C) for less than 1.5 h before being imaged with cTDM. The blood sample was diluted 1:4000 in phosphate-buffered saline containing 1% (wt/vol) of bovine serum albumin and gently placed on a glass slide to allow RBCs to settle on the surface. Five hundred interference images were captured at a speed of 180 fps under incident angles equally distributed within the ±65 deg range to obtain the 3-D RI tomogram of an RBC. About 15 RBCs were imaged for each subject, and the measurements took about 1 h. All of the experiments were performed at room temperature.

2.3 *RBC Segmentation from 3-D RI Maps*

We proposed an adaptive volume segmentation method, 3-D adaptive region-growing (3D-ARG), to delineate the precise

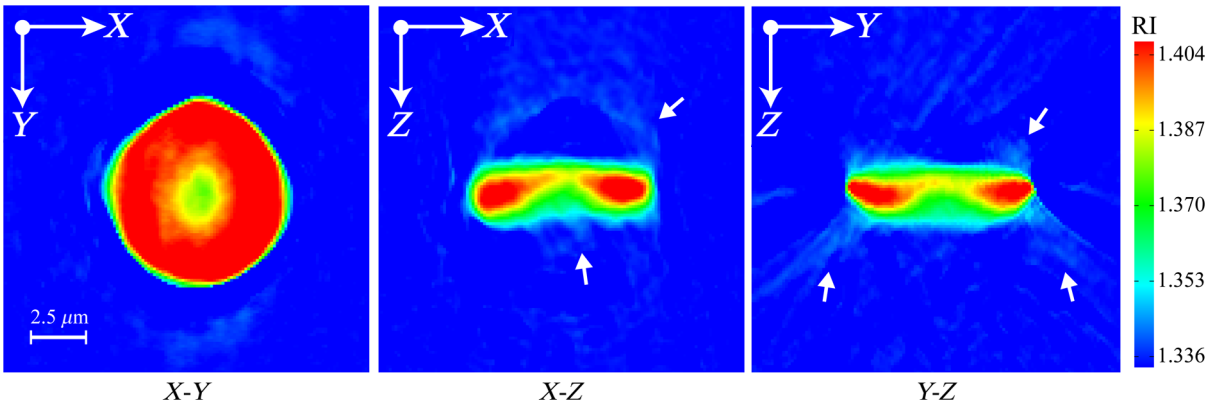

Fig. 1 Orthogonal views of an RBC reconstructed from cTDM data. Some artifacts (white arrows) are clearly visible after the reconstruction.

3-D contour of RBCs automatically. 3D-ARG combines the steps of volume scaling and Otsu's thresholding with 3-D region growing (Fig. 2). The volume scaling technique was implemented to improve the computation efficiency of region growing, and Otsu's thresholding was used to accelerate the selection of the seed region. The main segmentation method, 3-D region growing, was implemented to delineate the area of an RBC from its 3-D RI map as precisely as possible.

Volume scaling is a resampling technique in computer vision. Based on the concept of multiresolution representation, trilinear interpolation was used as the scaling kernel to reduce the size of 3-D RI maps and expand the segmentation masks hierarchically until the finest resolution was achieved. This method has an advantage of significantly reducing the computational cost and complexity. In this study, the scaling level was set to three to promote efficiency and avoid the oversmooth problem.

Otsu's method is a clustering-based image thresholding algorithm that calculates the optimal threshold in separating the foreground (sample) and background (medium) areas with the minimum within-class variance[29]

$$\sigma_w^2(t) = w_b(t)\sigma_b^2(t) + w_f(t)\sigma_f^2(t), \tag{1}$$

where w and σ^2 denote the weight and variance of the background (b) and foreground (f) separated by a threshold t, respectively. Otsu's thresholding was implemented as an initial step to obtain a rough sample region from 3-D RI maps at the smallest matrix size.

After the Otsu's method separated the two classes demonstrating a roughly bimodal histogram, the coordinate of the centroid, $C(x, y, z)$, was estimated from the separated foreground by

$$C(x, y, z) = \frac{1}{n}\sum_{i=1}^{n} c(x, y, z), \tag{2}$$

where $c(x, y, z)$ denotes the coordinates of the foreground region and n is the total number of foreground voxels.

3-D region growing is a region-based segmentation method.[30] The first delineation was formed by continuously growing from the seed point C to adjacent voxels that were in the initial foreground found by Otsu's thresholding. Any unconnected artifacts can be eliminated at this step. Subsequently, the second and final delineation masks were made by growing from the voxels selected by the previous delineation. Whether or not to grow to adjacent voxels was determined by the RI difference between the voxel of interest and the maximum value in the Otsu's foreground region. Based on our experience, the maximum RI range of RBCs is ~0.02. Therefore, the criterion for growing was set such that the RI of the newly connected

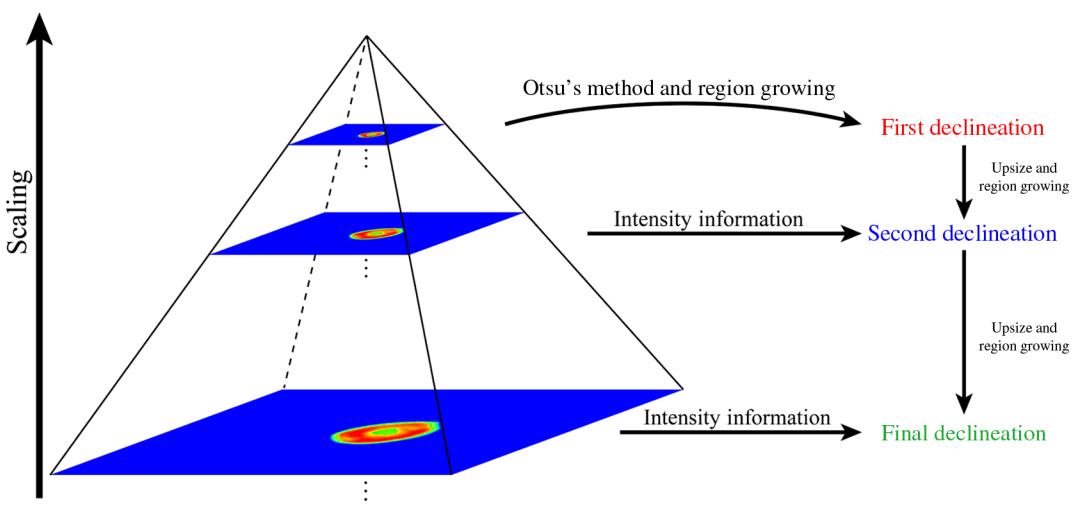

Fig. 2 The flowchart of 3D-ARG.

voxel should be within 0.02 of the maximum RI in the initial foreground region.

2.4 *Calculation of Optical Indices and Geometric Indices*

We measured the projection area and OV of each RBC from its phase image measured under normal incidence of the illumination beam. After reconstructing and delineating the 3-D RI map of an RBC, we calculated its average RI (RI_{avg}) from a 0.39-μm-thick slice around the focal plane to alleviate the problem of reduced RI near the cell boundary due to lower axial resolution. From the delineated 3-D mask of an RBC, $f(x,y,z)$, we obtained the contour and the total number of voxels identified as the RBC. Subsequently, we calculated the surface-area-to-volume ratio (S/V), where S is the surface area and V is the volume. The sphericity index (SI) is expressed as

$$SI = \frac{\pi^{1/3}(6V)^{2/3}}{S}. \tag{3}$$

In addition, changes of the RBC thickness with the radial position can be used to assess the cellular shape. To analyze the thickness distribution, we constructed a 2-D thickness map $T(x,y)$ [shown in Fig. 3(a)] from $f(x,y,z)$ by counting the number of voxels along the optical axis of the objective lens (i.e., z-axis)

$$T(x,y) = \sum_{z=0}^{z_{\max}} f(x,y,z). \tag{4}$$

The centroid of the RBC was obtained from $f(x,y,z)$ using Eq. (2) and projected onto the x-y plane. We estimated the thickness as a function of the radial position along various radial directions. The radial position of a pixel in $T(x,y)$ was defined as its distance from the projection of the RBC centroid in the x-y plane, normalized to the distance between the projection of the centroid and the boundary of $T(x,y)$ in the corresponding direction to compensate for any irregular cellular shape. Finally, we averaged the thickness distributions over all radial directions to obtain an average radial distribution of the thickness, as shown in Fig. 3(b). To evaluate the biconcave shape of RBCs, we defined an index Δ_{75} to describe the difference between the central thickness and the thickness at three quarters of the normalized radial position

$$\Delta_{75} = \frac{T_{75} - T_0}{T_{\text{avg}}}, \tag{5}$$

where T_{avg} is the average thickness of the entire RBC, T_{75} is the average thickness at 75% of the normalized radial position, and T_0 is the thickness at the centroid of the RBC. The effective radius of the RBC (R_{avg}) was derived by averaging the distances between the projection of the centroid and the boundary of $T(x,y)$ over all radial directions.

2.5 *Evaluation of the 3D-ARG Segmentation Method*

To evaluate the agreement/differences between the manual delineation and the automatic 3D-ARG segmentation, linear regression and Bland–Altman plots were used to analyze six morphological features extracted directly from 3-D RI maps. The performance of each of the features in distinguishing between healthy and thalassemic RBCs was evaluated using receiver operating characteristic (ROC) curves. To further enhance the prediction power, we used logistic regression (LR) to combine multiple optical and morphological indices and build a prediction model with the highest probability of distinguishing thalassemia. The most relevant parameters were selected using a

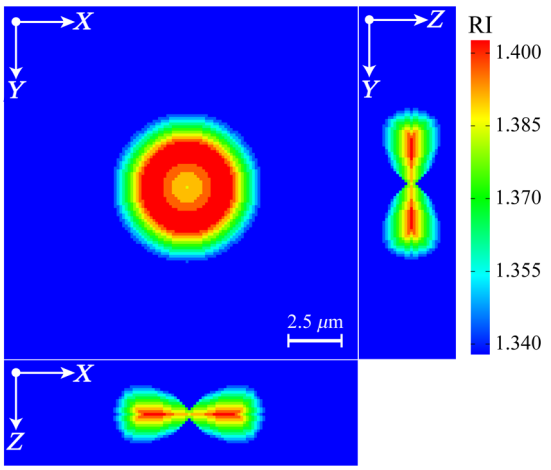

Fig. 4 The digital RBC phantom based on Cassini model. The volume is 87 fL, and the diameter is 7 μm.

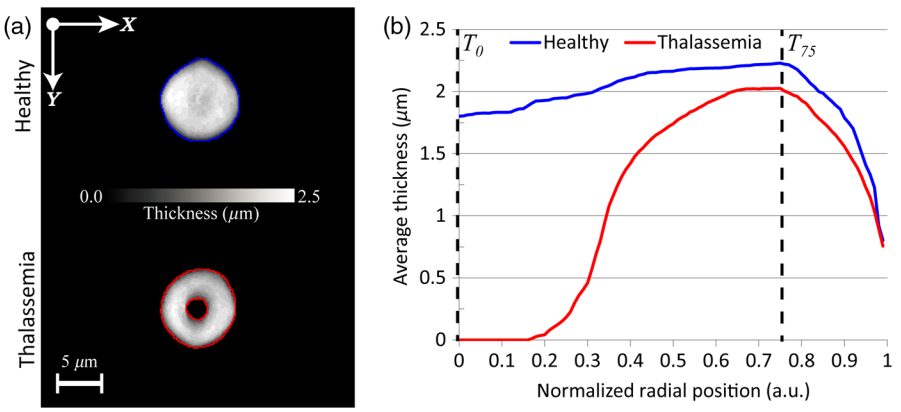

Fig. 3 Illustration of different thickness distributions of a healthy RBC and a thalassemic RBC. (a) Thickness maps and (b) radial distribution of the thickness.

sequential forward search based on the p-values for the goodness-of-fit test associated with diagnostic results. Predictive performances of various classifiers were evaluated using the area under the ROC curve (AUC). All the statistical analyses were performed with MedCalc (MedCalc software, Mariakerke, Belgium) in this study.

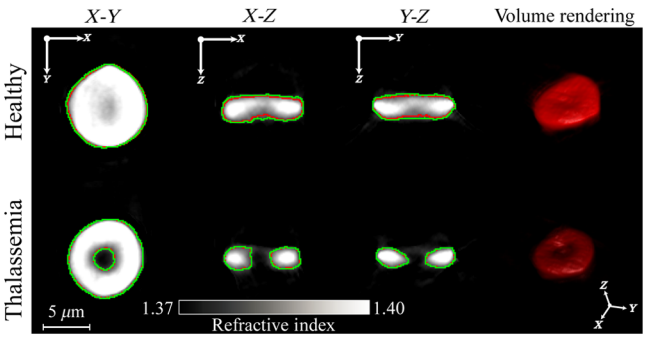

Fig. 5 Comparison of delineation results between manual delineation (red lines) and 3D-ARG (green lines) and the volume rendering of a healthy and a thalassemic RBC. The three selected orthogonal planes intersect at the centroid of the RBCs.

3 Results

3.1 *Validation of Three-Dimensional Adaptive Region Growing*

To evaluate the accuracy of segmentation by 3D-ARG, we constructed a 3-D digital RBC phantom based on Cassini ovals.[31] In Cartesian coordinates, the contour of the digital phantom in the x-z plane is described by

$$(x^2 + z^2 + a^2)^2 - 4a^2(x^2) = b^4. \tag{6}$$

To generate a Cassini oval, two focal points separated by a distance of $2a$ are set initially in the x-z plane. The contour of the oval consists of every point in the x-z plane that has the product of its distances to the two foci equal to b^2. Finally, the contour is rotated around the z-axis by 180 deg to generate the oval surface. In this study, the RI of voxels in the phantom was

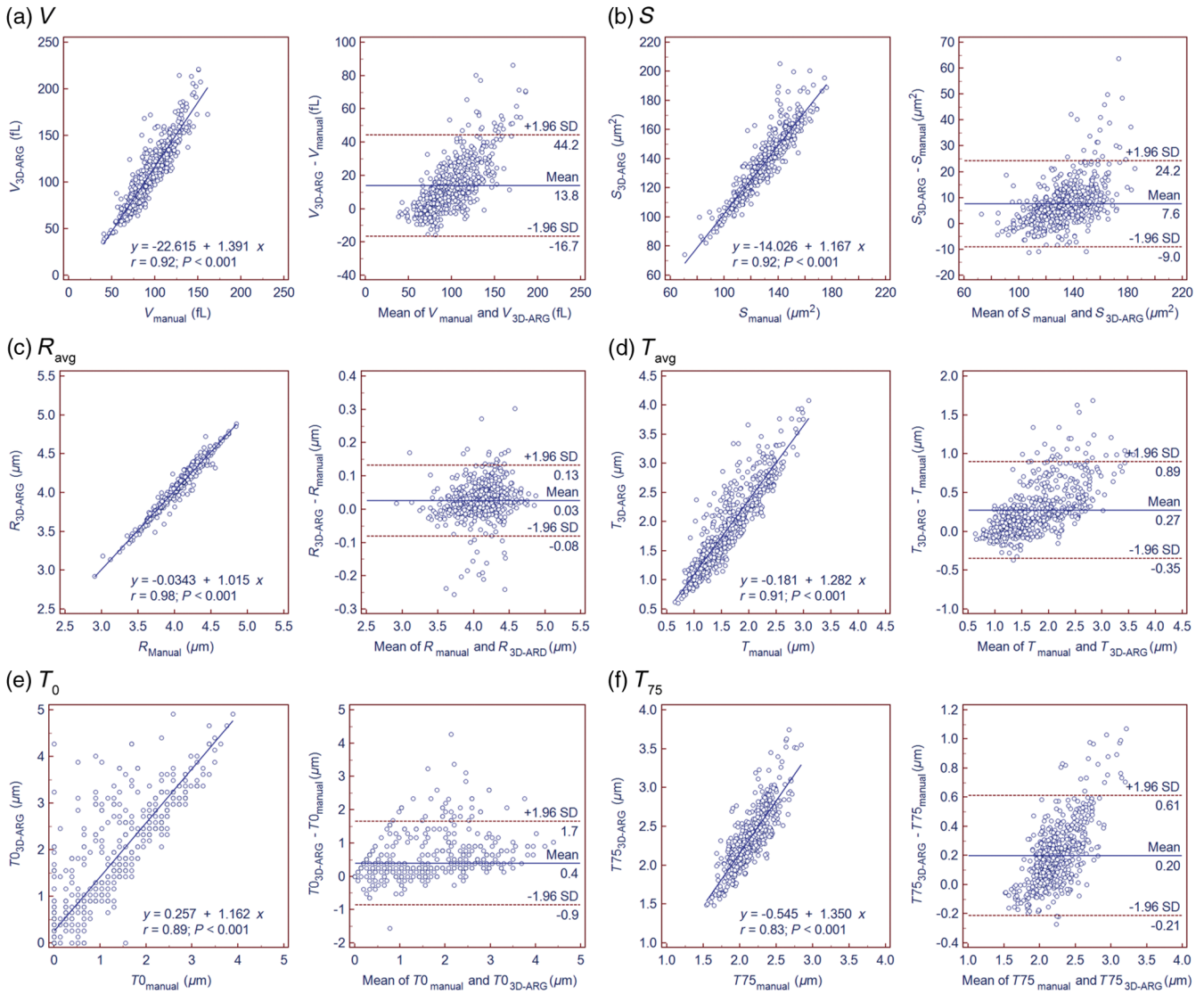

Fig. 6 Scatter plots and Bland–Altman plots for (a) volume, (b) surface area, (c) effective radius, (d) average thickness, (e) central thickness, and (f) average thickness at the normalized radial position of 0.75 to compare manual delineation with 3D-ARG delineation.

assigned to be in the range of 1.340 to 1.400 and increasing from the periphery to the center. The RI of the outside medium was set to be 1.340 (Fig. 4). The volume of the RBC phantom measured from the 3D-ARG segmentation result was 87 fL, which is the same as the expected value according to Eq. (6).

3.2 *Evaluation of the Accuracy of the 3D-ARG Method*

The contours of RBCs delineated using the 3D-ARG method were compared with those delineated manually (MD). Figure 5 shows orthogonal sections of 3-D RI maps of representative healthy and thalassemic RBCs. The contouring results are presented in red (MD) and green (3D-ARG) lines. For both healthy and thalassemic RBCs, the segmentation results agree with each other well. The results of quantifying morphological parameters from 3D-ARG segmented RBCs were highly consistent with those from manually segmented RBCs, as shown in scatter plots (Fig. 6) and summarized in Tables 1 and 2. Three derived indices including S/V, SI, and Δ_{75} are also listed in the tables. Results of linear regression showed excellent

Table 1 Morphometrics of normal RBCs extracted from manual delineation (MD) and 3D-ARG delineation results ($n = 172$).

Parameter	Mean ± SD	95% CI	Minimum	Maximum
V (fL)				
MD	111 ± 19	109 to 114	68	161
3D-ARG	129 ± 31	124 to 133	67	221
S (μm^2)				
MD	136 ± 13	134 to 138	104	169
3D-ARG	144 ± 16	142 to 147	105	189
R_{avg} (μm)				
MD	4.17 ± 0.20	4.14 to 4.20	3.62	4.74
3D-ARG	4.21 ± 0.21	4.17 to 4.24	3.63	4.87
T_{avg} (μm)				
MD	2.1 ± 0.4	2.0 to 2.1	1.2	3.1
3D-ARG	2.4 ± 0.6	2.3 to 2.5	1.0	4.1
T_0 (μm)				
MD	1.7 ± 1.0	1.6 to 1.9	0.0	3.9
3D-ARG	2.3 ± 1.2	2.1 to 2.4	0.0	4.9
T_{75} (μm)				
MD	2.2 ± 0.2	2.2 to 2.3	1.9	2.8
3D-ARG	2.5 ± 0.0	2.5 to 2.6	1.8	3.8
S/V (μm^{-1})				
MD	1.24 ± 0.132	1.22 to 1.26	0.973	1.58
3D-ARG	1.16 ± 0.170	1.14 to 1.19	0.826	1.70
SI				
MD	0.824 ± 0.053	0.816 to 0.832	0.723	0.947
3D-ARG	0.845 ± 0.065	0.835 to 0.855	0.698	1.01
Δ_{75}				
MD	0.3 ± 0.6	0.3 to 0.4	−0.4	1.7
3D-ARG	0.2 ± 0.6	0.1 to 0.3	−0.3	1.7

Note: SD, standard deviation; CI, confidence interval for the mean; MD, manual delineation; 3D-ARG, three-dimensional adaptive region growing.

Table 2 Morphometrics of thalassemic RBCs extracted from manual delineation (MD) and 3D-ARG delineation results ($n = 419$).

Parameter	Mean ± SD	95% CI	Minimum	Maximum
V (fL)				
MD	85 ± 18	84 to 87	40	147
3D-ARG	98 ± 29	95 to 101	36	215
S (μm^2)				
MD	127 ± 17	125 to 128	71	176
3D-ARG	134 ± 21	132 to 136	104	205
R_{avg} (μm)				
MD	4.03 ± 0.30	4.00 to 4.06	2.91	4.85
3D-ARG	4.05 ± 0.30	4.02 to 4.08	0.90	4.89
T_{avg} (μm)				
MD	1.4 ± 0.4	1.4 to 1.5	0.7	2.9
3D-ARG	1.7 ± 0.6	1.6 to 1.7	0.8	3.7
T_0 (μm)				
MD	0.5 ± 0.8	0.4 to 0.6	0.0	3.4
3D-ARG	0.8 ± 1.2	0.7 to 1.0	0.0	4.3
T_{75} (μm)				
MD	2.1 ± 0.2	2.1 to 2.1	1.5	2.7
3D-ARG	2.3 ± 0.3	2.2 to 2.3	1.4	3.5
S/V (μm^{-1})				
MD	1.51 ± 0.175	1.50 to 1.53	1.03	2.25
3D-ARG	1.43 ± 0.240	1.41 to 1.45	0.889	2.30
SI				
MD	0.739 ± 0.055	0.733 to 0.744	0.621	0.965
3D-ARG	0.759 ± 0.071	0.752 to 0.766	0.600	0.986
Δ_{75}				
MD	1.3 ± 0.7	1.2 to 1.4	−0.6	2.5
3D-ARG	1.1 ± 0.8	1.0 to 1.2	−0.6	2.6

Note: SD, standard deviation; CI, confidence interval for the mean; MD, manual delineation; 3D-ARG, three-dimensional adaptive region growing.

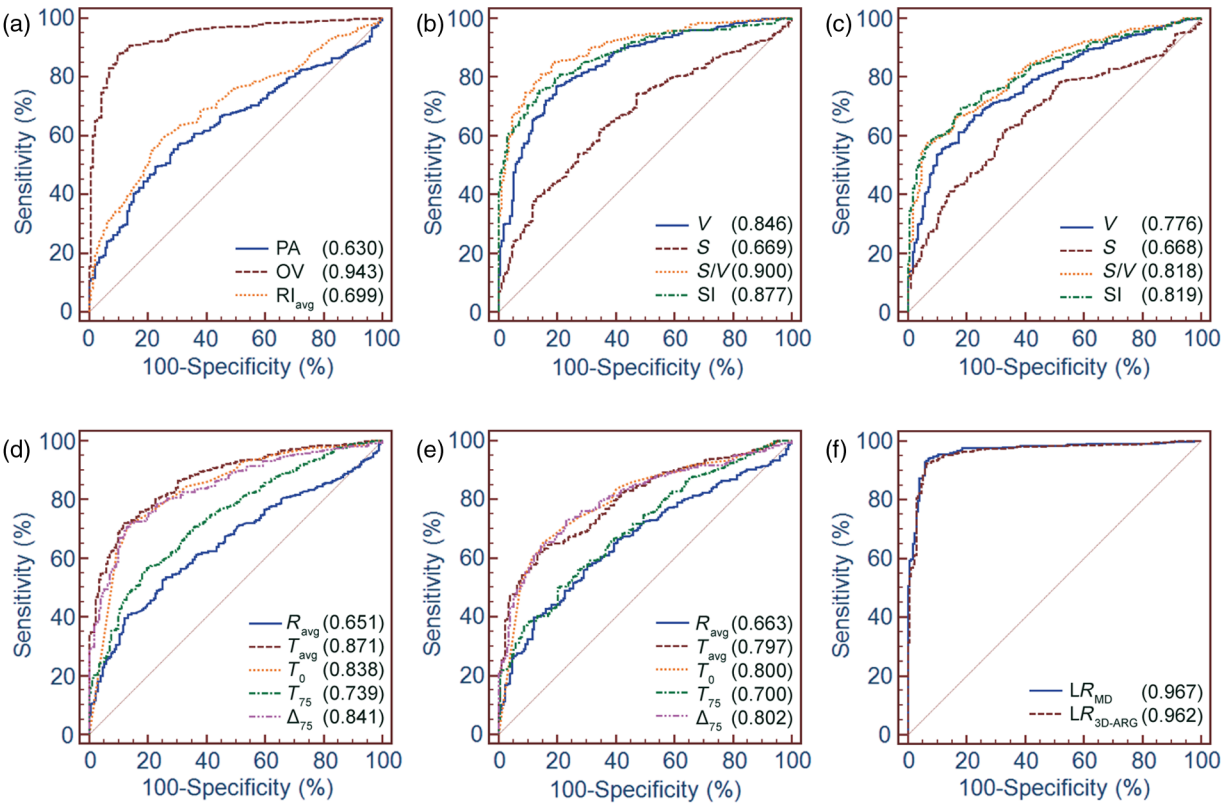

Fig. 7 ROCs curves of (a) projection area (PA), OV and RI_{avg}, (b, d) morphological indices extracted from 3-D RI maps with manual delineation, (c, e) morphological indices extracted from 3-D RI maps with 3D-ARG delineation, and (f) LR models for detecting individual RBCs with the two delineation methods. The closer the curve is to the upper left corner, the better the diagnostic performance is.

correlations between the 3D-ARG and the MD results for all the parameters (Pearson's correlation coefficients: V, 0.92; S, 0.92; R_{avg}, 0.98; T_{avg}, 0.91; T_0, 0.89; T_{75}, 0.83; S/V, 0.84; SI, 0.83; and Δ_{75}, 0.86. All of the p-values of F-tests were less than 0.001). Bland–Altman analysis revealed that the 3D-ARG segmentation systematically overestimated the morphological indices directly obtained from 3-D RI maps, including V (14 ± 16 fL), S (8 ± 9 μm^2), R_{avg} (0.03 ± 0.05 μm), T_{avg} (0.3 ± 0.3 μm), T_0 (0.4 ± 0.6 μm), and T_{75} (0.2 ± 0.2 μm).

3.3 *Performances of Various Indices to Distinguish Thalassemia*

Both of the optical indices, OV and RI_{avg}, revealed significant differences between patients and normal subjects. Results of OV measurements were 4.3 ± 0.7 fL for thalassemic RBCs and 5.9 ± 0.7 fL for healthy subjects (Student's t-test: $p < 0.001$), suggesting that the hemoglobin content of thalassemic subjects was 27% lower than that of healthy subjects. RI_{avg} also demonstrated a significant difference between thalassemic and healthy RBCs (1.389 ± 0.008 versus 1.395 ± 0.006; Student's t-test: $p < 0.001$).

The ROC curves for classifying individual thalassemic RBCs are shown in Fig. 7 with the corresponding AUC listed in parentheses. Table 3 summarizes the diagnostic performance of the evaluated indices on a per-cell basis. It can be seen that OV achieved the highest accuracy of detecting thalassemia (AUC > 0.9). The S/V and SI also demonstrated excellent ability to distinguish thalassemia (AUC > 0.8). The best multi-indices models built by LR included four indices: OV, S/V, SI, and S. The models are characterized by the following linear equations:

$$p_{\text{manual}}(x) = -143.14 - 0.24 \times \text{OV} + 42.73 \times S/V + 85.14 \times SI + 0.26 \times S, \quad (7)$$

$$p_{\text{3D-ARG}}(x) = -45.32 - 0.26 \times \text{OV} + 17.90 \times S/V + 26.01 \times SI + 0.13 \times S. \quad (8)$$

For classifying individual RBCs, AUCs of the two models with MD and 3D-ARG were 0.967 and 0.962, respectively. The diagnostic accuracy was 93.57% and 92.73%, respectively. Since in a clinical setting multiple RBCs can be imaged and a diagnosis is to be reached for each subject, we also evaluated the accuracy of diagnosing thalassemia with various indices on a per-subject basis; the results are summarized in Table 4. The diagnostic accuracy of both the OV and LR models achieved 100% for both manual and 3D-ARG segmentations.

Table 3 Comparison of diagnostic performance on individual RBCs.

Parameter	Sensitivity (%)	Specificity (%)	PPV (%)	NPV (%)	Accuracy (%)	AUC
Projection area	57.04	67.44	81.02	39.19	60.07	0.630
OV	87.83	91.86	96.33	75.60	89.00	0.943
RI_{avg}	60.38	73.79	86.94	39.19	63.83	0.699
V						
MD	76.85	80.23	90.45	58.72	77.83	0.846
3D-ARG	67.06	77.33	87.81	49.08	70.05	0.776
S						
MD	63.48	63.95	81.09	41.82	63.62	0.669
3D-ARG	62.05	66.86	82.02	41.97	63.45	0.668
S/V						
MD	80.91	85.47	93.13	64.76	82.24	0.900
3D-ARG	57.76	93.6	95.65	47.63	68.19	0.818
SI						
MD	75.42	86.05	92.94	58.97	78.51	0.877
3D-ARG	69.45	81.98	90.37	52.42	73.10	0.819
R_{avg}						
MD	52.74	75.00	83.71	39.45	59.22	0.651
3D-ARG	39.86	87.79	88.83	37.47	53.81	0.663
T_{avg}						
MD	71.6	88.37	93.75	56.09	76.48	0.871
3D-ARG	62.29	86.05	91.58	48.37	69.20	0.797
T_0						
MD	71.36	86.63	92.86	55.39	75.80	0.838
3D-ARG	65.39	84.88	91.33	50.17	71.06	0.800
T_{75}						
MD	55.37	81.98	88.21	42.99	63.11	0.739
3D-ARG	50.6	79.07	85.48	39.65	58.89	0.700
Δ_{75}						
MD	72.08	86.05	92.64	55.85	76.15	0.841
3D-ARG	73.27	76.74	88.47	54.10	74.28	0.802
LR model						
MD	95.47	88.95	95.46	88.96	93.57	0.967
3D-ARG	95.23	86.63	94.55	88.17	92.73	0.962

Note: PPV, positive predictive value; NPV, negative predictive value; MD, manual delineation; 3D-ARG, three-dimensional adaptive region growing; LR, logistic regression.

Table 4 Comparison of diagnostic performance on a per-subject basis.

Parameter	Sensitivity (%)	Specificity (%)	PPV (%)	NPV (%)	Accuracy (%)	AUC
Projection area	74.07	85.71	95.24	46.15	76.47	0.783
OV	100	100	100	100	100	1.000
RI_{avg}	70.37	85.71	95.00	42.86	73.53	0.786
V						
MD	100	85.71	96.43	100	97.06	0.947
3D-ARG	81.48	85.71	95.65	54.54	82.35	0.852
S						
MD	51.85	100	100	35.00	61.76	0.783
3D-ARG	62.96	85.71	94.44	37.50	67.64	0.725
S/V						
MD	100	85.71	96.43	100	97.06	0.968
3D-ARG	92.59	85.71	96.15	74.99	91.17	0.921
SI						
MD	96.30	85.71	96.30	85.73	94.12	0.952
3D-ARG	88.89	85.71	96.00	66.67	88.24	0.926
R_{avg}						
MD	70.37	100	100	46.67	76.47	0.794
3D-ARG	59.26	100	100	38.89	67.65	0.804
T_{avg}						
MD	100	85.71	96.43	100	97.06	0.952
3D-ARG	85.19	85.71	95.83	60.01	85.30	0.884
T_0						
MD	88.89	85.71	96.00	66.67	88.24	0.931
3D-ARG	88.89	85.71	96.00	66.67	88.24	0.905
T_{75}						
MD	85.19	71.43	92.00	55.56	82.36	0.804
3D-ARG	70.37	71.43	90.48	38.46	70.59	0.735
Δ_{75}						
MD	92.59	85.71	96.15	74.99	91.17	0.937
3D-ARG	92.59	85.71	96.15	74.99	91.17	0.937
LR model						
MD	100	100	100	100	100	1.000
3D-ARG	100	100	100	100	100	1.000

Note: PPV, positive predictive value; NPV, negative predictive value; MD, manual delineation; 3D-ARG, three-dimensional adaptive region growing; LR, logistic regression.

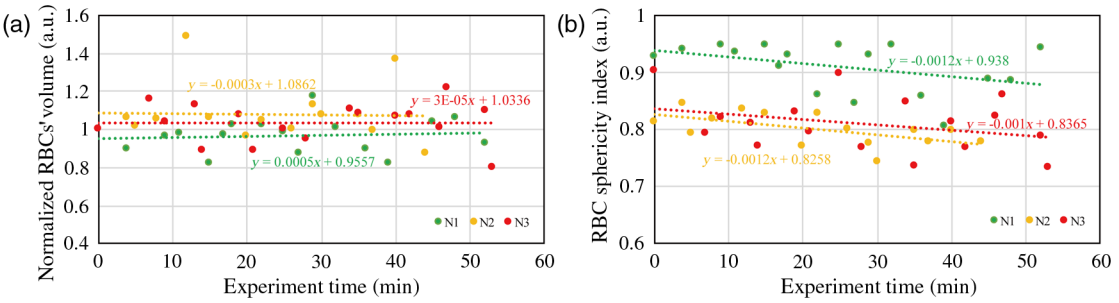

Fig. 8 Illustration of the (a) normalized volume and (b) sphericity index of RBCs from three volunteers over time of measurement.

4 Discussion and Conclusion

We successfully demonstrated that the developed 3D-ARG method enables automatic extraction of morphological parameters of RBCs from 3-D RI maps acquired with cTDM. Compared with the manual contouring performed by a physician, the 3D-ARG segmentation method overestimates the V, S, R_{avg}, T_{avg}, T_0, and T_{75} of the RBCs (Fig. 6 and Tables 1–2). There are two main reasons that may have caused the minor estimation bias in the morphological measurements. First, speckle noise intrinsic to cTDM due to the high spatial coherence of the light source introduces errors in both the amplitude and phase of the measured scattered field, causing artifacts after reconstruction.[32] Second, the axial resolution is relatively large (1 μm) due to the incomplete coverage of projection angles[28] and aberrations generated by optical components such as the high numerical-aperture objective lens. Despite these limitations, the results demonstrate that the developed 3D-ARG is a reliable automatic segmentation tool for distinguishing thalassemic RBCs from normal RBCs with an accuracy comparable to the time-consuming manual delineation by an expert physician. In addition, 3D-ARG has the advantage of quantifying various 3-D morphological indices rapidly from the delineation results rather than estimating parameters via 2-D QPI planimetry.[20–22]

As summarized in Tables 1 and 2, average values of morphological indices of healthy subjects including the V, S, R_{avg}, T_{avg}, T_0, and T_{75} are significantly higher than those of thalassemic patients (Student's t-test: $p < 0.001$). This phenomenon can be attributed to the smaller size of thalassemic RBCs than healthy ones. In addition, the thalassemic RBCs have significantly larger S/V and Δ_{75} and significantly smaller SI than normal ones (Student's t-test: $p < 0.001$). The differences in the three shape-related indices reflect the fact that the 3-D RI maps of most thalassemic RBCs are doughnut-shaped as shown in Figs. 3 and 5. The elevated S/V of thalassemic RBCs may indicate abnormalities in cell volume regulation and deformability. It is worth mentioning that for normal RBCs a larger S/V is likely to promote efficiency in the exchange of oxygen and carbon dioxide. However, the deficient hemoglobin content of microcytic RBCs in thalassemic patients still causes hypoxia of tissues.[33]

The AUC results in Tables 3 and 4 demonstrate that OV is the best single index to distinguish thalassemia. If contributions of other constituents of an RBC to the RI are ignored, OV is proportional to the dry mass of hemoglobin, which equals the average hemoglobin concentration multiplied by the volume of an RBC. The results of RI_{avg} show that thalassemic RBCs have significantly smaller average RI than healthy RBCs, indicating reduced hemoglobin concentrations in thalassemic RBCs. Since both the hemoglobin concentration and the volume decrease in thalassemic RBCs, OV augments the difference between normal and thalassemic RBCs and thus is well suited for distinguishing between healthy and thalassemic RBCs.

The LR method shows excellent performance in distinguishing thalassemic from healthy RBCs since it utilizes an optimal set of features to build the prediction model. As shown in Table 3, combining multiple indices improved the diagnostic accuracy of distinguishing individual thalassemic RBCs, compared with just using a single index. This demonstrates the major advantage of supplementing cTDM with 3D-ARG to automatically obtain 3-D morphological features of RBCs for comprehensive characterization of cellular shape and size. Because causes of various blood-related diseases differ, the method demonstrated in this paper has the potential to discriminate other blood disorders as well. Sickle cell disease, for example, is characterized by RBCs with significantly abnormal shapes and slightly different hemoglobin contents.[11] The hereditary spherocytosis is another blood disease with normal hemoglobin content and abnormal membrane structure.[17] We believe that building a multi-indices model based on automatically segmented 3-D RI maps of RBCs is a viable strategy for obtaining the optimal combination of morphological indices to better distinguish blood diseases than only using indices extracted from 2-D phase images or a single index.

Other high-resolution imaging techniques, such as the scanning electron microscopy (SEM), confocal microscopy, and third-harmonic generation (THG) microscopy, are also capable of visualizing the shape of RBCs at high spatial resolution.[34–36] SEM has an order of magnitude higher spatial resolution, but the cell fixation and labeling processes are time consuming and may alter the shape of cells. Obtaining 3-D images of RBCs using confocal microscopy or THG is time-consuming because of the required point-scanning process. In addition, the cost of a femtosecond laser source required for THG imaging is prohibitively high for clinical examinations. cTDM is more cost effective and better suited to providing 3-D morphological information of unstained living cells almost in their natural state. In addition, the hemoglobin content can be obtained simultaneously from the 2-D phase image acquired under normal incidence of the illumination beam.

Since living RBCs were analyzed in the study, it is necessary to discuss effects of dynamic changes in cellular morphology. First, to find out whether there is significant change in RBC volume during the 1 h measurement time, we analyzed the correlation between the volume and measurement time of RBCs in data acquired from three healthy volunteers. In each dataset, the extracted RBC volumes were normalized to the volume of the

first measured RBC, as shown in Fig. 8(a). Since the slopes of linear regression approach zero, we conclude that no apparent change in the RBC volume was observed during the 1 h measurement time. Interestingly, Fig. 8(b) demonstrates that the *SI* of RBCs in the three datasets decreased by an average of 7% in 1 h. This might be caused by gradual flattening of RBCs on the glass slide. Second, the flicking of the RBC membrane at the time scale of 2 s is related to biophysical properties of the membrane[37] and has been quantified with QPI to range from 49 to 60 nm.[16] Considering the thickness of healthy RBCs being about 2 μm, the flicking causes less than 3% fluctuations in the volume. Therefore, it was ignored in this study. Whether the morphological dynamics provide additional information for diagnostics requires further research.

The reconstruction method used in the study assumes the Rytov approximation, which is limited to weakly scattering objects with a low phase gradient and works independently of the object size.[14,38] The validity condition of applying the Rytov approximation to optical diffraction tomography of biological cells has been discussed in Refs. 38 and 39. In summary, the local variation of RI in an object over the length scale of wavelength, Δn, needs to be much less than one. In the results of the current study, the maximum Δn in an RBC is in the range of 0.032 to 0.061. Therefore, it is appropriate to apply the Rytov approximation. In addition, human erythrocytes lack cell nucleus and organelles and mainly consist of hemoglobin uniformly distributed in the cytoplasm. Since the purpose of this study is to distinguish healthy and thalassemic erythrocytes via the morphometric analysis, the detailed structure of RBCs such as cell membrane is ignored. Previous studies on light scattering properties of biological cells[40] and RBCs[41] have shown that the scattering strength of cells is dominated by forward scattering, and backward scattering (i.e., a scattering angle larger than 90 deg) is more sensitive to RI fluctuations with sizes similar to or smaller than the wavelength. To confirm that collecting scattered fields with scattering angles below 65 deg is sufficient to reconstruct RI tomograms of RBCs for morphometric analysis, we estimated the angular scattering intensity distribution of RBCs by the finite-difference time-domain method,[42] using the RI tomogram of a representative RBC obtained in the study. We found that the forwardly scattered light in the scattering angle range below 65 deg accounted for 99.99% of the total scattering.

In conclusion, we successfully developed an automatic segmentation method for extracting RBCs from 3-D RI maps acquired with cTDM and demonstrated significant differences in morphometric features between healthy and thalassemic RBCs without staining. The multivariable LR method shows perfect accuracy for distinguishing between healthy subjects and patients with thalassemia. With the tiny amount of blood sample required and convenient label-free 3-D imaging capability, we believe that this technique could be beneficial for screening thalassemia in newborns. In addition, using cTDM with the newly developed automatic segmentation tool has the potential to identify other blood diseases associated with abnormal hemoglobin content and/or morphology of RBCs and to facilitate the 3-D morphometric analysis of RBCs in these diseases.

Disclosures

All authors state that they have no relevant financial interests in this article and no other conflicts of interest to disclose.

Acknowledgments

The authors thank the National Health Research Institutes (Grant No. NHRI-EX102- 10020EC) and Ministry of Science and Technology (Grant No. 102-2221-E-002-032-MY3) in Taiwan for financial support.

References

1. M. Diez-Silva et al., "Shape and biomechanical characteristics of human red blood cells in health and disease," *MRS Bull.* **35**(5), 382–388 (2010).
2. G. Dhaliwal, P. A. Cornett, and L. M. Tierney Jr., "Hemolytic anemia," *Am. Fam. Physician* **69**(11), 2599–2606 (2004).
3. D. G. Silva et al., "Oxidative stress in sickle cell disease: an overview of erythrocyte redox metabolism and current antioxidant therapeutic strategies," *Free Radical Biol. Med.* **65**, 1101–1109 (2013).
4. M. Schrier and L. Stanley, "Thalassemia: pathophysiology of red cell changes," *Annu. Rev. Med.* **45**(1), 211–218 (1994).
5. P. M. S. Roma et al., "Total three-dimensional imaging of phase objects using defocusing microscopy: application to red blood cells," *Appl. Phys. Lett.* **104**(25), 251107 (2014).
6. K. V. Gilev et al., "Advanced consumable-free morphological analysis of intact red blood cells by a compact scanning flow cytometer," *Cytometry A* **91**(9), 867–873 (2017).
7. K. V. Gilev et al., "Mature red blood cells: from optical model to inverse light-scattering problem," *Biomed. Opt. Express* **7**(4), 1305–1310 (2016).
8. D. Dannhauser et al., "Optical signature of erythrocytes by light scattering in microfluidic flows," *Lab. Chip.* **15**(16), 3278–3285 (2015).
9. M. Kugeiko and D. Smunev, "Method for determining erythrocyte surface area by polarization and nephelometric measurements," *J. Appl. Spectrosc.* **82**(6), 985–992 (2016).
10. G. Popescu et al., "Imaging red blood cell dynamics by quantitative phase microscopy," *Blood Cells Mol. Dis.* **41**(1), 10–16 (2008).
11. H. Byun et al., "Optical measurement of biomechanical properties of individual erythrocytes from a sickle cell patient," *Acta Biomater.* **8**(11), 4130–4138 (2012).
12. M. T. Rinehart, H. S. Park, and A. Wax, "Influence of defocus on quantitative analysis of microscopic objects and individual cells with digital holography," *Biomed. Opt. Express* **6**(6), 2067–2075 (2015).
13. R. Barer, "Interference microscopy and mass determination," *Nature* **169**(4296), 366–367 (1952).
14. K. Kim et al., "High-resolution three-dimensional imaging of red blood cells parasitized by *Plasmodium falciparum* and in situ hemozoin crystals using optical diffraction tomography," *J. Biomed. Opt.* **19**(1), 011005 (2014).
15. H. Park et al., "3-D refractive index tomograms and deformability of individual human red blood cells from cord blood of newborn infants and maternal blood," *J. Biomed. Opt.* **20**(11), 111208 (2015).
16. S. Lee et al., "Refractive index tomograms and dynamic membrane fluctuations of red blood cells from patients with diabetes mellitus," *Sci. Rep.* **7**, (2017).
17. Y. Kim et al., "Profiling individual human red blood cells using common-path diffraction optical tomography," *Sci. Rep.* **4**, 6659 (2014).
18. P. Hosseini et al., "Cellular normoxic biophysical markers of hydroxyurea treatment in sickle cell disease," *Proc. Natl. Acad. Sci. U. S. A.* **113**(34), 9527–9532 (2016).
19. N. T. Shaked et al., "Quantitative microscopy and nanoscopy of sickle red blood cells performed by wide field digital interferometry," *J. Biomed. Opt.* **16**(3), 030506 (2011).
20. F. Yi et al., "Automated segmentation of multiple red blood cells with digital holographic microscopy," *J. Biomed. Opt.* **18**(2), 026006 (2013).
21. I. Moon et al., "Automated statistical quantification of three-dimensional morphology and mean corpuscular hemoglobin of multiple red blood cells," *Opt. Express* **20**(9), 10295–10309 (2012).
22. F. Yi, I. Moon, and Y. H. Lee, "Three-dimensional counting of morphologically normal human red blood cells via digital holographic microscopy," *J. Biomed. Opt.* **20**(1), 016005 (2015).
23. F. Yi, I. Moon, and B. Javidi, "Cell morphology-based classification of red blood cells using holographic imaging informatics," *Biomed. Opt. Express* **7**(6), 2385–2399 (2016).

24. W. C. Hsu et al., "Tomographic diffractive microscopy of living cells based on a common-path configuration," *Opt. Lett.* **39**(7), 2210–2213 (2014).
25. G. Popescu et al., "Diffraction phase microscopy for quantifying cell structure and dynamics," *Opt. Lett.* **31**(6), 775–777 (2006).
26. P. Girshovitz and N. T. Shaked, "Fast phase processing in off-axis holography using multiplexing with complex encoding and live-cell fluctuation map calculation in real-time," *Opt. Express* **23**(7), 8773–8787 (2015).
27. M. A. Schofield and Y. Zhu, "Fast phase unwrapping algorithm for interferometric applications," *Optics Lett.* **28**(14), 1194–1196 (2003).
28. J. W. Su et al., "Digital holographic microtomography for high-resolution refractive index mapping of live cells," *J. Biophotonics* **6**(5), 416–424 (2013).
29. N. Otsu, "A threshold selection method from gray-level histograms," *IEEE Trans. Syst. Man. Cybern. Syst.* **9**(1), 62–66 (1979).
30. R. Adams and L. Bischof, "Seeded region growing," *IEEE Trans. Pattern. Anal. Mach. Intell.* **16**(6), 641–647 (1994).
31. J. Hellmers, E. Eremina, and T. Wriedt, "Simulation of light scattering by biconcave Cassini ovals using the nullfield method with discrete sources," *J. Opt. A Pure Appl. Opt.* **8**(1), 1 (2005).
32. W. Krauze et al., "Generalized total variation iterative constraint strategy in limited angle optical diffraction tomography," *Opt. Express* **24**(5), 4924–4936 (2016).
33. D. H. Chui, S. Fucharoen, and V. Chan, "Hemoglobin H disease: not necessarily a benign disorder," *Blood* **101**(3), 791–800 (2003).
34. B. Rappaz et al., "Comparative study of human erythrocytes by digital holographic microscopy, confocal microscopy, and impedance volume analyzer," *Cytometry A* **73**(10), 895–903 (2008).
35. I. Saytashev et al., "Multiphoton excited hemoglobin fluorescence and third harmonic generation for non-invasive microscopy of stored blood," *Biomed. Opt. Express* **7**(9), 3449–3460 (2016).
36. B. Blasi et al., "Red blood cell storage and cell morphology," *Transfus. Med.* **22**(2), 90–96 (2012).
37. Y. Park et al., "Light scattering of human red blood cells during metabolic remodeling of the membrane," *J. Biomed. Opt.* **16**(1), 011013 (2011).
38. Y. Sung et al., "Optical diffraction tomography for high resolution live cell imaging," *Opt. Express* **17**(1), 266–277 (2009).
39. P. Müller, M. Schürmann, and J. Guck, "The theory of diffraction tomography," arXiv:1507.00466 (2015).
40. R. Drezek, A. Dunn, and R. Richards-Kortum, "A pulsed finite-difference time-domain (FDTD) method for calculating light scattering from biological cells over broad wavelength ranges," *Opt. Express* **6**(7), 147–157 (2000).
41. L. Bi and P. Yang, "Modeling of light scattering by biconcave and deformed red blood cells with the invariant imbedding T-matrix method," *J. Biomed. Opt.* **18**(5), 055001 (2013).
42. G. S. Chao and K. B. Sung, "Investigating the spectral characteristics of backscattering from heterogeneous spherical nuclei using broadband finite-difference time-domain simulations," *J. Biomed. Opt.* **15**(1), 015007 (2010).

Yang-Hsien Lin received his BS degree in biomedical imaging and radiological science from China Medical University, Taiwan, in June 2011 and his MS degree in biomedical imaging and radiological science from the National Yang-Ming University, Taiwan, in 2013. Currently, he is working toward his PhD in biomedical electronics and bioinformatics at the National Taiwan University. His research interests include developments and applications of the optimization of tomographic phase microscopy and three-dimensional imaging.

Shin-Shyang Huang received his BS degree in radiological sciences from the National Yang-Ming University, Taiwan, in 2014 and his MS degree in biomedical electronics from the National Taiwan University, Taiwan, in 2016. His research interests include developments and applications of optical microscopy.

Shang-Ju Wu received his PhD in clinical medicine from the National Taiwan University. He joined the Department of Internal Medicines at the National Taiwan University Hospital in 2001. His research fields include lymphoblastic leukemia, myeloid leukemia, and stem cell transplantation.

Kung-Bin Sung received his MS degree and PhD in biomedical engineering from the University of Texas at Austin in 1999 and 2003, respectively. He worked as a research scientist at Intel Corporation from 2003 to 2006. He joined the Department of Electrical Engineering and Graduate Institute of Biomedical Electronics and Bioinformatics at the National Taiwan University in 2006. His research focuses on developing optical spectroscopy and microscopy techniques for early diagnosis of cancer and precancer.